

CIRCULATION COPY
SUBJECT TO RECALL
IN TWO WEEKS

UCRL- 84021
PREPRINT

MULTIPLE-LINE THERMAL BLOOMING, STRONG
 t^3 -BLOOMING, AND PHASE COMPENSATION
CALCULATIONS WITH FOUR-D

J. R. Morris
J. A. Fleck, Jr.

This paper was prepared for submittal to
the High Energy Laser Propagation, Adaptive
Optics Meeting at the Army Missile Command,
Redstone Arsenal, Alabama, 19-20 March 1980.

March 1980



Lawrence
Livermore
Laboratory

This is a preprint of a paper intended for publication in a journal or proceedings. Since changes may be made before publication, this preprint is made available with the understanding that it will not be cited or reproduced without the permission of the author.

DISCLAIMER

This document was prepared as an account of work sponsored by an agency of the United States Government. Neither the United States Government nor the University of California nor any of their employees, makes any warranty, express or implied, or assumes any legal liability or responsibility for the accuracy, completeness, or usefulness of any information, apparatus, product, or process disclosed, or represents that its use would not infringe privately owned rights. Reference herein to any specific commercial product, process, or service by trade name, trademark, manufacturer, or otherwise, does not necessarily constitute or imply its endorsement, recommendation, or favoring by the United States Government or the University of California. The views and opinions of authors expressed herein do not necessarily state or reflect those of the United States Government or the University of California, and shall not be used for advertising or product endorsement purposes.

MULTIPLE-LINE THERMAL BLOOMING, STRONG t^3 -BLOOMING,
AND PHASE COMPENSATION CALCULATIONS WITH FOUR-D

J. R. Morris and J. A. Fleck, Jr.

Lawrence Livermore Laboratory, University of California
Livermore, California 94550

Abstract

FOUR-D's steady-state multiple-line mode was used to evaluate a power-weighted-average model of NACL beam propagation. Five NACL lines were propagated with separate intensity, phase, wavelength, and absorption coefficient. The on-target areas obtained from a power-weighted average model were up to 36% smaller than the corresponding multiple-line model areas. The maximum difference occurred for pure diffraction and decreased as thermal blooming was increased.

The FOUR-D strong t^3 -blooming model combines an exact solution of the linearized hydrodynamic equations with a steady-state model of overlap blooming. Propagation of a focused high-power multipulse laser beam with a uniformity illuminated square aperture demonstrates the generality of this model. In the examples, the square beam outperformed the Gaussian beam by 20-40% in peak intensity, 55-80% in half-power area. The contribution of t^3 -blooming to the on-target area was decreased by overlap blooming for the Gaussian beam, but increased for the square beam.

Two of FOUR-D's three models of phase compensation for steady-state thermal blooming -- an effective thin lens and return wave -- will also be discussed.

*Work performed under the auspices of the U. S. Department of Energy by Lawrence Livermore Laboratory under contract #W-7405-ENG-48 and for the U.S. Army Missile Research and Development Command under contract #W31-U31-93-8577.

I. INTRODUCTION

FOUR-D is a wave-optics code for simulating the propagation of high-energy laser beams through the atmosphere. For coplanar scenarios, development of the steady-state and time-dependent isobaric sections of FOUR-D began in 1974 under ARPA and MICOM funding. Initially FOUR-D was used to simulate time-dependent propagation through stagnation zones.¹ In 1975-6 under Navy and MICOM funding the steady-state flow was upgraded to two-dimensional to permit simulation of noncoplanar scenarios; multipulse steady-state overlap blooming and triangular pulse t^3 -blooming models were added during this time.² Since 1976, under MICOM funding, a strong t^3 -blooming model, a general steady-state multiple line propagation model, and several phase compensation models have been developed and added to FOUR-D.^{3,4} During this period FOUR-D has been used to simulate a number of propagation problems of interest to the Army including propagation of the ABEL and NACL laser beams.

FOUR-D employs a split-operator finite fourier propagation algorithm that is second order accurate (in Δz) for thermal blooming and n -th order accurate for diffraction. Approximate solutions to the linearized hydrodynamics equations that describe the density of heated air in and near the laser beam are provided for all important parameter regimes, for example, subsonic steady-state, supersonic steady-state, time-dependent isobaric, and full time-dependent (within short pulses). Transverse wind fields whose direction is a function of the distance from the laser (noncoplanar scenarios) are modeled by the steady-state and strong t^3 -blooming sections of FOUR-D. Turbulence, high frequency jitter, and low frequency jitter models are also in FOUR-D.

FOUR-D includes a number of features that enhance its utility as a "full-up" propagation code. An adaptive propagation step allows the thermal blooming to be accurately modeled where the laser beam or wind field is changing rapidly without wasting time where both are changing slowly. An adaptive lens transformation permits most problems to be run without first making an accurate estimate of the on-target area. A non-diffraction limited beam model permits simulation of beams with random initial phase imperfections. Finally, measured intensity and phase profiles can be used to provide accurate simulation of real laser beams.

FOUR-D handles a wide range of hydrodynamic flow conditions. For strong t^3 -blooming a solution to the complete set of three hydrodynamic equations during the time of a single pulse is coupled to a steady state model of overlap blooming. Time-dependent thermal blooming is treated using the isobaric approximation for one-dimensional wind fields. Steady-state thermal blooming is treated for two-dimensional wind fields by a Fourier method for subsonic winds and by integration along characteristics for supersonic winds.

The remainder of this paper is divided into three sections. Section II briefly reviews the LLL multiple line laser model and compares multiple line and power-weighted average simulations of NACL beam propagation. Section III describes a comparison between strong t^3 -blooming of a square and of a Gaussian beam in the presence of significant overlap blooming. Finally, section IV describes two of the three models of phase compensation for thermal blooming that exist in FOUR-D.

II. MULTIPLE-LINE AND POWER-WEIGHTED-AVERAGE PROPAGATION OF THE NACL BEAM

A. The LLL Multiple Line Laser Model

The power of high energy DF lasers is distributed over more than five spectral lines. Corresponding to each of these lines there may be a separate spatial-gain distribution in the active medium that gives rise to a unique intensity and phase profile at the output of the optical train. For such lasers, if these intensity and phase profiles are sufficiently dissimilar the simple power-weighted average-absorption coefficient model² may not adequately model propagation.

FOUR-D has the most general steady-state model of multiple line laser propagation currently available.⁵ Each line can have its own intensity profile, phase profile, wavelength, and absorption coefficient. Furthermore, the new model can simulate the propagation of either CW or multipulse (without t³ blooming) beams in coplanar or noncoplanar scenarios.

The general multiline propagation algorithm closely parallels the time-dependent propagation algorithm described in earlier reports.^{1,2} Each line or time sample is propagated using the basic split-operator algorithm:

$$\begin{aligned} \mathcal{E}_i(z + \Delta z) = & \exp \left(- i \frac{\Delta z}{4k_i} \nabla_1^2 \right) \exp (i\phi_i) \\ & \exp \left(- i \frac{\Delta z}{4k_i} \nabla_1^2 \right) \mathcal{E}_i(z) \end{aligned} \quad (1)$$

The first and third exponential operators in Eq. (1) represent vacuum propagation steps; the second is a phase screen that accounts for atmospheric heating between z and $z + \Delta z$.

During the vacuum propagation steps, each field sample propagates independently whether it represents a spectral line or a time sample. Only the phase-screen computation is different for the two algorithms. However, even here there is a close parallel between time-dependent and multiline calculations, as is illustrated in Fig. 1. Both algorithms start by computing the intensity that corresponds to each electric-field sample. In the multiline calculation the net heat deposit rate, $\Sigma \alpha_i I(x, \lambda_i)$, is used to calculate the steady-state density change; in the time-dependent calculation the instantaneous heating rate, $\alpha I(x, t_i)$, is used to update the isobaric approximation to the density from t_{i-1} to t_i . In both cases the density change is used to compute the phase change for each line or time-sample. For the time-dependent calculation there is a different density for each time-sample but a single ratio between density change and phase change; for the multiline calculation there is only one density but a slightly different ratio of phase-change to density for each line caused by line-to-line wavelength differences.

B. Description of Data and Single Line Diffraction

The simulations of NACL beam propagation described here are based on one single line and one five line set of Wavefront Analyzer (WFA) data set supplied to us by Carl Larson at the Naval Surface Weapons Center (NSWC). The single line data set was taken at 3.875μ . The five line data set was taken at 3.837μ , 3.875μ , 3.800μ , 3.927μ , and 3.965μ in a series of five successive NACL runs. The intensity and phase data in both sets were averages over twenty successive WFA frames or 0.2 sec.

The data was provided as a multiple frame average because the NACL intensity and phase fluctuated so rapidly that single frame values were not representative of the long time behavior of the LASER. A 10-20 frame average intensity is more suitable than a single frame intensity for thermal blooming in Army scenarios because at the laser the air is heated during a wind clearing time of 0.14-0.355 sec for transverse wind speeds of 2-5 m/sec.

Using a time-averaged phase is more questionable; however, it represents the best that can be done with the existing data. Since the WFA is a scanning instrument, single frame phases are not representative of the actual field when significant frame-to-frame fluctuations exist. Carl Larson of NSWC⁶ computed an estimate of the effect of using the average phase. He found that for vacuum propagation over a 20 frame time period the area obtained by propagating individual frames and computing an average intensity in the focal plane was 1.6-1.9 times larger than the area obtained by propagating the 20 frame average electric field.

For the five line data set, we used a power distribution over the 5 lines that corresponded directly to the intensities in the data set without modification, since all 5 lines were measured with the same attenuation factor. This results in a model that is reasonable, but has most of the power from unsimulated lines added to the 3.875 μ line.

For both data sets, the near field coordinate system of the WFA was expanded by a factor of 5.7 to obtain a beam size approximating that of the NACL beam at the Navy Pointer-Tracker output aperture.⁶

Our computations indicate that the beam quality of the NACL laser at the WFA aperture was improved by approximately 30% between the two measurements of

the 3.875 μ line supplied to us. This improvement is evident in both the far-field intensities and in the near-field phases. Figure 2 compares the calculated far-field intensities for those focal lengths that minimize the 63.2% power area at a range of 1 km. The area for the early data is 13.2 cm^2 ; for the more recent data, 6.1 cm^2 (a 54% decrease) -- a perfect phase front would further reduce this area to 3.4 cm^2 . Table 1 describes the improvement in the near-field phase by comparing the Zernike coefficients obtained from an intensity-weighted least-squares fit. The more recent data has astigmatism, primary coma, and trifol coma coefficients whose magnitude are 43%, 19%, and 31%, respectively, of the corresponding coefficients for the early data. The refocus coefficient of the recent data is 4.9 times that of the early data, but focus and tilt are easily corrected so a best correction for each data set was used in the calculation of Figure 2.

C. Diffraction of the Multiple Line and an effective Single Line Model of the NACL Laser Beam

The effective single line model of the the NACL beam, which is discussed in this section, is formed from the total intensity of the multiple line data set and the phase of the 3.837 μm line (an arbitrary choice). This model is used for all the power-weighted average thermal blooming calculations discussed in the next section. The calculations described in this section show that the effective single line model underestimates the on-target area in the absense of thermal blooming by 36% and thereby suggest that power-weighted average blooming calculations for low to moderate blooming of the NACL laser beam will not be very accurate (unless some ad hoc adjustments are applied to the phase data).

The intensities at the laser are shown for both models of the NACL beam in Fig. 3. The distribution of power over the backwards "C" intensity profile of the NACL laser varies significantly from line to line. The intensity of the 3.80 μm line is almost a vertical bar while that of the 3.875 μm line is a fully formed "C". The intensity for the single line model (total intensity) is similar to the intensity of the 3.875 μm line which has about one-third of the total power in our model; it is somewhat broader and considerably more uniformly filled "C" than most of the true single line intensity profiles.

In the multiple line model, each line has its own phase, as measured by the WFA. The coefficients of an intensity-weighted least-squares fit of a Zernike polynomial expansion to the phase of each line, shown in Table 2, indicate that the line-to-line phase variation is substantial, especially for the tilt, refocus, and astigmatism. The largest vector difference in the tilt coefficients occurs between the 3.80 μm and the 3.927 μm lines; its magnitude, 6.55, corresponds to 13 μrad of pointing error. The refocus coefficients correspond to a +0.3 to -6.4 m displacement of the Gaussian focal plane at 1 km range. (For comparison, an elliptical Gaussian beam approximately the size of the NACL beam [70 cm major axis diameter at the $e^{-2} I_{pk}$ intensity contour and a ratio of major to minor axes of 3] doubles in area at 15 m from a 1 km focus.) The maximum and minimum astigmatism coefficients, if taken alone, would displace the principal focal lines 14 m and 8.6 m from each other; the transverse orientation of the principal focal lines differs by 0.54 radian in the worst case. The coma coefficients are close enough in value that a coma correction should be effective; the magnitudes are within 33% of each other while the maximum difference between the transverse orientations of

the principal axes is 0.57 radians for primary coma and 0.14 radians for tri-foil coma.

For diffraction without thermal blooming the effective single line and the more correct multiple line models of the NACL laser beam give similar on-target isointensity contour patterns at 1 and 3 km range, but actual areas that differ by approximately 36% of the more correct multiple line value. Figure 4 illustrates this for diffraction to 1 km with the spherical focus term of the initial phase adjusted independently to give the smallest on-target area for each model. Most of the 16.8 cm^2 and 10.7 cm^2 areas obtained with the multiple line and the effective single line models, respectively, are due to imperfect phase; with a perfect spherical focusing phase, these areas decrease to 1.63 cm^2 and 1.01 cm^2 respectively. The ratio of the area obtained with the effective single line model to that obtained with the multiple line model is almost the same for measured phase and perfect phase calculations - 0.64 for measured phase and 0.62 for perfect phase; thus the NACL intensity and phase distributions contribute to the difference between the results of the two models in direct proportion to their relative importance in each model alone.

D. Multiple Line and Power-Weighted Average Calculations of Thermal Blooming of the NACL Laser Beam

Figure 5 describes the three coplanar approach scenarios for the thermal blooming calculations discussed in this section. Two of the scenarios have 1 km range and one has 3 km range. The distances of closest approach are 62.5 m and 250 m for the 1 km scenarios and 250 m for the 3 km scenario. A 2m/sec

wind perpendicular to the linear target trajectory creates a transverse component of air flow relative to the laser beam of between 1.94 and 2.00 m/sec at the laser. The slewing numbers are moderate to large: 10.7 and 39.0 for the 1 km calculations and 14.0 for the 3 km calculations. The slewing is into the wind so no stagnation zone occurs.

Table 3 summarizes the laser and atmospheric parameters. The absorption coefficients are from Long et.al.⁷ The scattering coefficient is a nominal value somewhat larger than twice the clear day, but less than half the hazy day, aerosol scattering coefficient computed by McClatchey;⁸ the slight wavelength dependence of this value is unimportant and has been neglected. The distribution of power among the lines has already been discussed; it is a reasonable description of the NACL beam, except that most of the power in lines for which data was not supplied has been placed in the 3.875 m line.

Unless otherwise stated the wind direction is perpendicular to the vertical bar of the backwards "C" NACL intensity profile and directed from vertical bar to the opening of the "C".

Figures 6-8 compare the on-target isointensity contours obtained from a multiple line (ML) calculation to that obtained from power-weighted average (PWA) calculation for each of the above three scenarios. For all three scenarios the ML intensity profile qualitatively resembles the PWA intensity profile in that both have high intensity heads, long low intensity tails, and similar horizontal to vertical aspect ratios. However, a quantitative comparison of on-target areas reveals significant differences between the ML and the PWA calculations. In all cases the PWA area is smaller; for the two scenarios at 1 km range it is 32.1 and 27.2% less than the ML area, for the

scenario at 3 km range it is 15.3% less than the ML area. Since the corresponding difference for diffraction alone is 36%, diffraction and geometric-optics effects are responsible for most of the difference between these ML and PWA calculations of NACL beam propagation. Thermal blooming actually reduces the percent difference between areas obtained from the ML and PWA models in the above three scenarios; ie, the more severe the thermal blooming, the more closely the ML and PWA calculations resemble each other.

The single line and fluence areas tabulated in Table 4 offer a clue as to why thermal blooming seems to moderate the difference between ML and PWA calculations for the NACL beam. The single line areas due to diffraction (lines 1 and 4 of Table 4) are all significantly smaller than the fluence area for each of these calculations. The substantial line-to-line tilt differences (and differences in higher aberrations) noted earlier have displaced the on-target centroids relative to each other so that the total intensity covers a larger area than the intensity of any single line. Thermal blooming increases the on-target area of each line thereby increasing the overlap of these areas. As it becomes large, thermal blooming swamps the effect of line-to-line pointing differences thereby reducing the relative error of the PWA model compared to the ML model.

The calculated effect of three different orientations of the NACL backwards "C" intensity relative to the wind direction is also shown in Table 4. Relative to the NACL beam as displayed in Figure 2 the wind direction was left (from the vertical ridge toward the mouth of the "C"), right, and vertical in the 3 cases. The largest difference (between the left and right wind directions) is principally an artifact of the data sets rather than

representative of the actual propagation of the NACL beam. Prior to entry into the WFA the NACL beam was dispersed through a grating rhomb which separated the intensity distributions by as much as several centimeters at the WFA input;⁶ when scaled by the 5.7 magnification factor used to approximate NPT output, this corresponds to the ~ 11 cm displacement between the 3.800 and 3.965 μ intensity distributions in our 5 line data set. Four of the five lines obey the rule that the farther downwind its ridge is the more it is degraded by thermal blooming; only the thermal blooming of the 3.927 μ line for the wind to the right case fails to follow this pattern. Correcting for the lateral dispersion shift would probably yield an on-target area between that of our calculations for left and right wind directions, i.e. between 500 and 680 cm^2 , and the differences between the areas of the lines would be reduced. The calculated area for the vertical wind direction is almost the same as for the wind to the left--even the single line areas match closely, except for that of the 3.967 μ line. This latter line is far enough down wind in our calculations (due to the uncorrected dispersion displacement) that changing the wind direction from left to vertical substantially reduces the heated air that this line sees from the other four lines. Correcting for the lateral dispersion displacement would increase the on-target areas for vertical wind because the initial distributions would be more closely superimposed, it would probably also reduce the differences between the on-target areas for the three wind directions, but detailed calculations are needed to verify this.

III. Self-Consistent Calculation of Strong t^3 -Blooming in the Presence of Significant Overlap Blooming

FOUR-D's multiple time-step model of strong t^3 -blooming allows it to calculate t^3 plus overlap blooming even in cases where t^3 -blooming drastically modifies the intensity of the laser beam late in the pulse. The overlap blooming is assumed to be steady-state so that each pulse is identical to the one that preceded it. Then, all the pulses can be represented by a single collection of electric field samples taken at equally spaced times within a representative pulse. The pulse duration is assumed to be short compared to the interpulse time so that overlap blooming can be calculated from an impulse or δ function approximation determined by the single pulse fluence and the overlap number. The interpulse time is also assumed to be long enough that the isobaric approximation to the hydrodynamic equations is valid for the overlap blooming.

The single pulse blooming is calculated using an exact solution of all three hydrodynamics equations. The only further assumption made is that at each point in the transverse spatial grid the intensity is adequately approximated by a continuous function of time that is piecewise linear. The generality of this solution makes it applicable to arbitrary beam profiles and makes single pulse blooming calculations (no overlap blooming) valid at arbitrary wind velocities. A complete description of the model can be found in ref. 3.

Comparison of Overlap Blooming Plus t^3 -Blooming of Square and Gaussian Beams

To illustrate the generality of the strong t^3 -blooming model, we have calculated t^3 -blooming for a single pulse and combined t^3 -blooming and overlap blooming for a steady-state multipulse beam, assuming that the beam is uniform in intensity over a square at $z = 0$. The laser-beam, atmospheric, and scenario parameters (Table 5) have been chosen to produce a substantial reduction (greater than a factor of two) in the on-target peak intensity owing to either overlap or single-pulse t^3 -blooming. The beam at $z = 0$ was apodized slightly and is displayed in Fig. 9.

The time-dependence of the on-target intensity for the first pulse in the train, which undergoes t^3 -blooming only, is shown in Fig. 10. The profile at $5 \mu s$ is very close to that of a diffraction-limited beam that has most of its power concentrated in the central lobe. At $10 \mu s$ the on-axis hole has started to develop and by $15 \mu s$ it is almost completely formed. This behavior, of course, also is exhibited when Gaussian beams undergo t^3 -blooming.

A comparison has been made between the single-pulse t^3 -blooming characteristics of a square beam and a Gaussian beam that have the same power and the same focal-plane peak half-power area in the absence of thermal blooming. Results of this comparison are given in line 2 of Table 6, where there is agreement within 10% for the time-averaged maximum intensity in the target plane of the two beams. This suggests that the amount of t^3 -blooming is roughly independent of beam shape for beams of the same power, provided they are of comparable size in the focal plane in the absence of thermal blooming.

Results for a typical pulse that has reached steady-state are shown in Fig. 11. In this case, the effects of both t^3 -blooming and overlap blooming are present. The focal-plane isointensity contours are shown for a uniform square beam at $z = 0$, corresponding to two values of the offset parameter. In both cases, the profiles at $5 \mu s$ are determined almost entirely by overlap blooming that occurs near the laser. At this time t^3 -blooming, which occurs primarily near the focal plane, has not yet had time to develop. The calculation for a 100 m offset has so much overlap blooming that it dominates the effect of t^3 -blooming, which at 10 and $15 \mu s$ merely spreads the intensity profile somewhat. The resulting single-pulse fluence profile thus resembles the "overlap only" profile. The 250 m offset calculation shows comparable amounts of t^3 -blooming and overlap blooming. By $10 \mu s$ the "overlap only" profile has been broadened and distorted significantly by t^3 -blooming. By $15 \mu s$, t^3 -blooming clearly dominates overlap blooming and there is scant resemblance of the intensity profile to the "overlap only" profile. Thus, t^3 -blooming and overlap blooming interact as though blooming occurs in two separate stages, with overlap blooming occurring near the laser and the resultant beam affected by t^3 -blooming near the focal plane.

The above calculations were repeated at the same power for a Gaussian beam at $z = 0$ adjusted to have (in the absence of thermal blooming) the same half-power area in the focal plane as the square beam. In Table 6, two performance measures, maximum intensity and minimum half-power areas, are compared for the two initial beam shapes. Results are included for t^3 -blooming alone, overlap blooming alone, and combined t^3 -blooming and overlap blooming. The

Gaussian beam shape leads to substantially greater beam degradation from overlap blooming alone than does the uniform square beam. This is not unexpected, as uniform beams tend to suffer less thermal blooming than do comparable Gaussian beams. The effect of t^3 -blooming alone reduces the on-target intensities by comparable amounts. The Gaussian beam gives a 10% higher peak intensity but a slightly larger half-power area than does the uniform square beam. The combined effect of t^3 -blooming and overlap blooming is very close to the effect of overlap blooming alone for the Gaussian beam. This is because overlap blooming substantially broadens the Gaussian beam, making subsequent t^3 -blooming relatively ineffective. The square beam, in contrast, suffers less overlap blooming, so that the beam-size is smaller where t^3 -blooming becomes effective. Consequently, the contribution of t^3 -blooming to the effect of combined overlap blooming and t^3 -blooming is greater for the uniform square beam than for the Gaussian beam. This comparison should hold also for a uniform beam of general shape. A significant difference between the two beam shapes in the case of combined blooming is that the square-beam on-target intensity profile is relatively compact, as indicated by the relatively modest increase in the product of area and peak intensity, while the Gaussian beam on-target intensity profile consists of a sharp peak superimposed on a broad low-intensity base, as indicated by the much larger product of area and peak intensity.

For the Gaussian beam overlap blooming broadens the beam area near the target and thereby decreases the effect of t^3 -blooming. The difference between the on-target areas for t^3 -blooming and overlap blooming alone is 2 cm^2 for 250 m offset, and -18 cm^2 for the 100 m offset (see Table 6).

For the square beam overlap blooming increases the effect of t^3 -blooming. The difference between the on-target areas for t^3 plus overlap blooming and overlap blooming alone is 17 cm^2 for 250 m offset and 11.3 cm^2 for 100 m offset. Both of these areas are greater than the 5 cm^2 difference between the area for t^3 blooming alone and the diffraction limited area. The cause of this unusual behavior is almost certainly that the square beam diffraction pattern has an on-axis hole near its focal plane which overlap blooming fills in. Concentrating the power near the axis for a longer distance from the focal (target) plane tends to increase t^3 -blooming.

IV. FOUR-D's Models of Phase Compensation for Thermal Blooming

FOUR-D contains three methods for calculating the effect of phase compensation for thermal blooming: a return wave algorithm for steady-state CW or multipulse overlap blooming,⁴ an equivalent thin-lens model,^{3,9} and the Bradley-Herrmann model¹⁰. Previous investigation^{3,9} has shown that the performance the Bradley-Herrmann model and the equivalent then lens model are similar while the latter has a wider range of applicability (to multipulse beams and in noncoplanar scenarios). A discussion of the Bradley-Herrmann is available in the open literature,¹⁰ so it will not be discussed further here.

Equivalent Thin-Lens Phase Compensation Model

The equivalent thin-lens model^{3,9} assumes that the thermally-bloomed laser beam at some distance z_a from the laser can be reproduced by a thin lens at the laser followed by vacuum propagation to z_a . The negative of this lens becomes the phase compensation for the first z_a km of the propagation path. The parameter z_a is adjusted to maximize the peak intensity or minimize the laser-beam area at the target.

The mathematical form of the above assumptions is

$$\mathcal{P}_L e^{i\psi} \mathcal{E}_0 = \mathcal{P}_{NL} \mathcal{E}_0$$

where \mathcal{P}_L is the linear diffraction operator for propagation over a distance z_a , $\mathcal{P}_{NL} \mathcal{E}_0$ is the thermally bloomed beam at z_a from the laser, and ψ is the estimate of the phase compensation to be applied to the initial field \mathcal{E}_0 .

Computation of ψ requires a single Fourier transform and no storage of phase fronts. Since a thermally-bloomed beam is larger than the corresponding diffraction-limited beam, the return beam is usually smaller than the original

uncorrected beam and easily fits inside the aperture grid. Once the optimum value of z_a has been determined, an improved correction may be obtainable by iterating to find a self-consistent heating distribution. However, experience shown that such additional iterations usually result in only marginal improvement.

Return-Wave Phase Compensation Model

FOUR-D also contains a model of return-wave phase compensation for steady-state thermal blooming of cw and multipulse laser beams. As the high-power laser beam is propagated to the target, each density calculation is saved in a disk file. Each density calculation is performed on an appropriate mesh determined by the adaptive-lens transformation best suited to the deformation of the high-power laser beam. The return-wave beam is initialized to a small Gaussian centered at the location of the peak intensity at the target; it is directed back along the incoming ray at this location by giving it the same tilt as the high-power laser beam at this point. The return-wave beam is propagated back to the laser aperture using the same lens transformation that is used to propagate the high-power beam to the target; this avoids interpolating the calculated densities because the return-beam mesh and the mesh the density is defined on are identical.

The diameter of the return-wave beam at the target is chosen to be the larger of the diffraction-limited beam diameter at the target (estimated with a Gaussian-beam formula) and a fraction of the smallest rms dimension of the high-power intensity profile at the target; the fraction used for the latter is an input parameter. The diffraction-limited diameter would be the ideal choice except for spatial aliasing; that is, sometimes the size must be increased to keep the return-wave confined within the computational mesh. The

second choice for the diameter of the return-wave beam at the target provides a means for controlling this spatial aliasing.

Figure 12 shows results of a representative return-wave calculation for multipulse laser beams under steady-state conditions with only overlap thermal blooming present. The upper row of iso-intensity contour plots corresponds to the uncorrected laser beam of 0.5, 0.75, and 1.0 times the distance to the target; the lower row of intensity profiles is for the phase-compensated beam at these same locations. The corrected peak intensity at the target is 98.6% of the corresponding diffraction-limited intensity. This steady-state result matches the result obtained by Wallace¹¹ for the same conditions using a time-dependent calculation.

Figures 13 and 14 illustrate steady-state return-wave phase compensation for thermal blooming of a cw Gaussian beam. Both of these calculations are for severe thermal blooming as can be seen from the plots of the uncorrected on-target intensity. In both cases the blooming was severe enough that successive iterations produced large changes in the on-target intensity and iso-intensity contours. In the $N_\omega = 30$ case of fig. 13 the on-target intensity appeared to converge. In the $N_\omega = 0$ of fig. 14 the on target intensity increased for the initial correction and the first iteration, but decreased in subsequent iterations; this behavior is due to the large contribution of the region near the target to cw thermal blooming at high power in a uniform wind.

Table 7 compares the performances of the return-wave algorithm and the equivalent thin-lens model.¹⁰ For these calculations the return-wave algorithm gives peak intensities and half-power areas that are typically

within 5-10% of the values obtained with the equivalent thin-lens model. Only for the calculation summarized on the second line did the return-wave algorithm significantly outperform the equivalent thin-lens model; the former gave a 14% smaller area and a 33% higher peak intensity at the target than the latter.

NOTICE

This report was prepared as an account of work sponsored by the United States Government. Neither the United States nor the United States Department of Energy, nor any of their employees, nor any of their contractors, subcontractors, or their employees, makes any warranty, express or implied, or assumes any legal liability or responsibility for the accuracy, completeness or usefulness of any information, apparatus, product or process disclosed, or represents that its use would not infringe privately-owned rights.

Reference to a company or product name does not imply approval or recommendation of the product by the University of California or the U.S. Department of Energy to the exclusion of others that may be suitable.

References

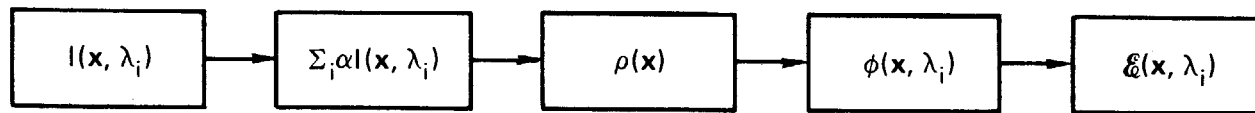
1. J. A. Fleck, Jr., J. R. Morris and M. D. Feit, Appl. Phys. 10, 129 (1976);
"Time-Dependent Propagation of High-Energy Laser Beams Through the
Atmosphere," Lawrence Livermore Laboratory Report UCRL-51826 (1975).
2. J. A. Fleck, Jr., J. R. Morris and M. D. Feit, Appl. Phys. 14, 99 (1977);
"Time Dependent Propagation of High-Energy Laser Beams Through the
Atmosphere: II", Lawrence Livermore Laboratory Report UCRL-52071 (1976).
3. J. R. Morris and J. A. Fleck, Jr., "Time-Dependent Propagation of
High-Energy Laser Beams Through the Atmosphere: III," Lawrence Livermore
Laboratory Report UCRL-52377 (1977).
4. J. R. Morris and J. A. Fleck, Jr., "Time-Dependent Propagations of
High-Energy Laser Beams Through the Atmosphere: IV," Lawrence Livermore
Laboratory Report UCRL-52654 (1978).
5. J. Herrmann has independently developed a similar model that he has used
to simulate propagation of the BDL Laser (private communication).
6. Carl Larson, Naval Surface Weapons Center (private communication, 1979).
7. R. K. Long, F. S. Mills, and G. L. Trusty, "Calculated Absorption
Coefficients for DF Laser Frequencies," Ohio State University
Electro-Science Laboratory Report RADC-TR-73-389 (1973).
8. R. A. McClatchey and J. E. A. Selby, "Atmospheric Attenuation of HF and DF
Laser Radiation," Air Force Cambridge Research Laboratories Report
AFCRL-72-0312 (1972).
9. J. A. Fleck, Jr. and J. R. Morris, Appl. Opt. 17, 2575 (1978).
10. L. C. Bradley and J. Herrmann, Appl. Opt. 13, 331 (1974).
11. J. Wallace and J. Pasciak, J. Opt. Soc. Am. 65, 1257 (1975).

FIGURE CAPTIONS

- Figure 1 Comparison of algorithms for multiple line steady-state calculations and time-dependent calculations.
- Figure 2 Comparison of on-target isointensity contour plots at 1 km range and 3.875μ wavelength from NACL runs taken about two months apart.
- Figure 3 Isointensity contours of individual NACL lines as used in our five line model plus the total intensity used in our power-weighted-average calculations.
- Figure 4 Comparison of multiple line and "power weighted average" on-target intensities due to diffraction alone. Both beams were adjusted for best focus.
- Figure 5 Schematic of coplanar scenarios for our NACL multiple line and power-weighted-average thermal blooming calculations.
- Figure 6 Comparisons of multiple line and power-weighted-average on-target isointensity contours for thermal blooming of the NACL beam in the 1 km scenario with the 250 m offset. Thermal blooming is light in this scenario.
- Figure 7 Comparison of multiple line and power-weighted average on-target isointensity contours for thermal blooming of the NACL beam in the 1 km scenario with the 62.5 m offset.
- Figure 8 Comparison of multiple line and power-weighted average on-target isointensity contours for thermal blooming of the NACL beam in the 3 km scenario. The offset was 250 m.

- Figure 9 Isointensity contour plot of square beam at the laser aperture showing the extent of edge and corner smoothing used in our calculations.
- Figure 10 Calculated time evolution of on-target intensity along the x-axis of square beam t^3 -blooming (no overlap). The intensities are scaled individually to emphasize the shape change.
- Figure 11 Calculated on-target isointensity contour plots for square beam t^3 plus overlap blooming.
- Figure 12 Evolution of isointensity contours with propagation distance for steady-state multipulse calculations: (a) without phase compensation, (b) with phase compensation. The dimensionless parameters of this calculation are $N_0 = 4$, $N_\omega = 0$, $N_F = 9.1$, $N_A = 0.4$, and $N_D = 17.8$.
- Figure 13 Isointensity contour plots at the target plane after successive iterations of return-wave phase compensation for thermal blooming of a Gaussian beam. The dimensionless parameters of this calculation are $N_F = 103$, $N_A = 0.12$, $N_\omega = 30$, and $N_D = 283$.
- Figure 14 Same as figure 13 except $N_\omega = 0$, $N_D = 16.2$. On the second iteration this calculation began diverging---on-target peak intensity decreased and on-target area increased.

Multiline



Time-dependent

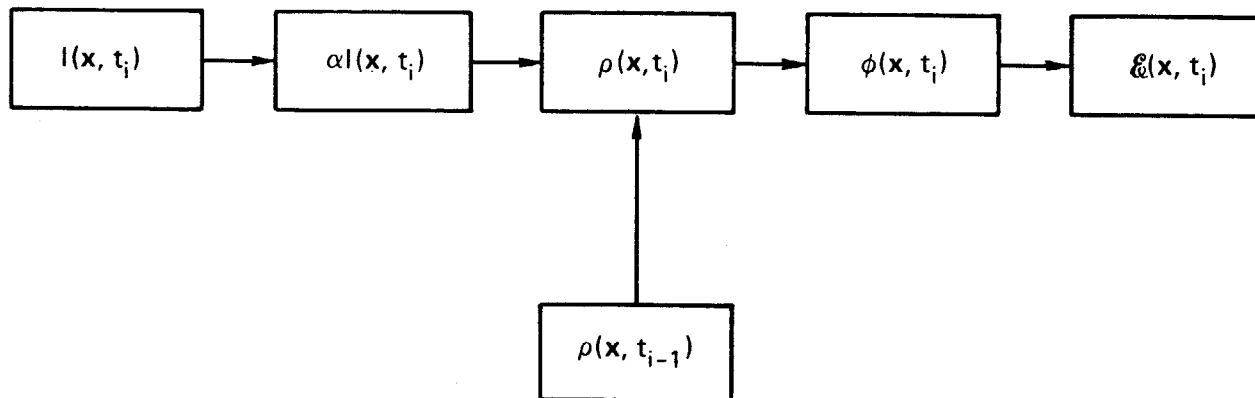
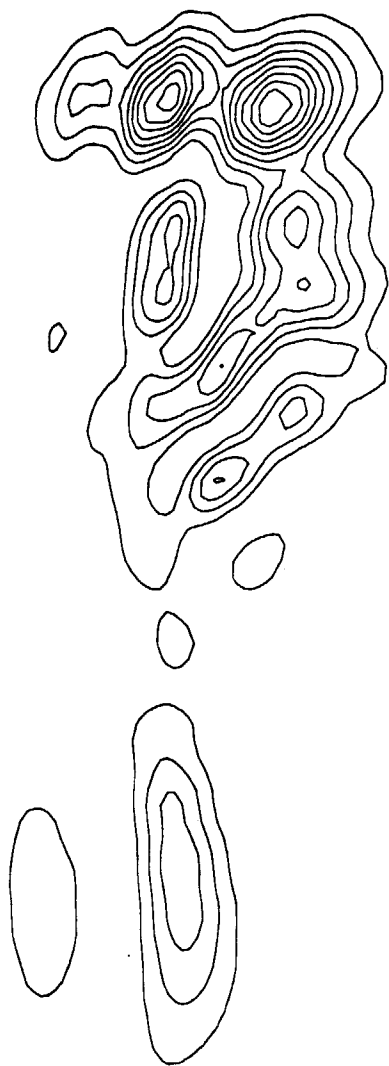


Figure 1

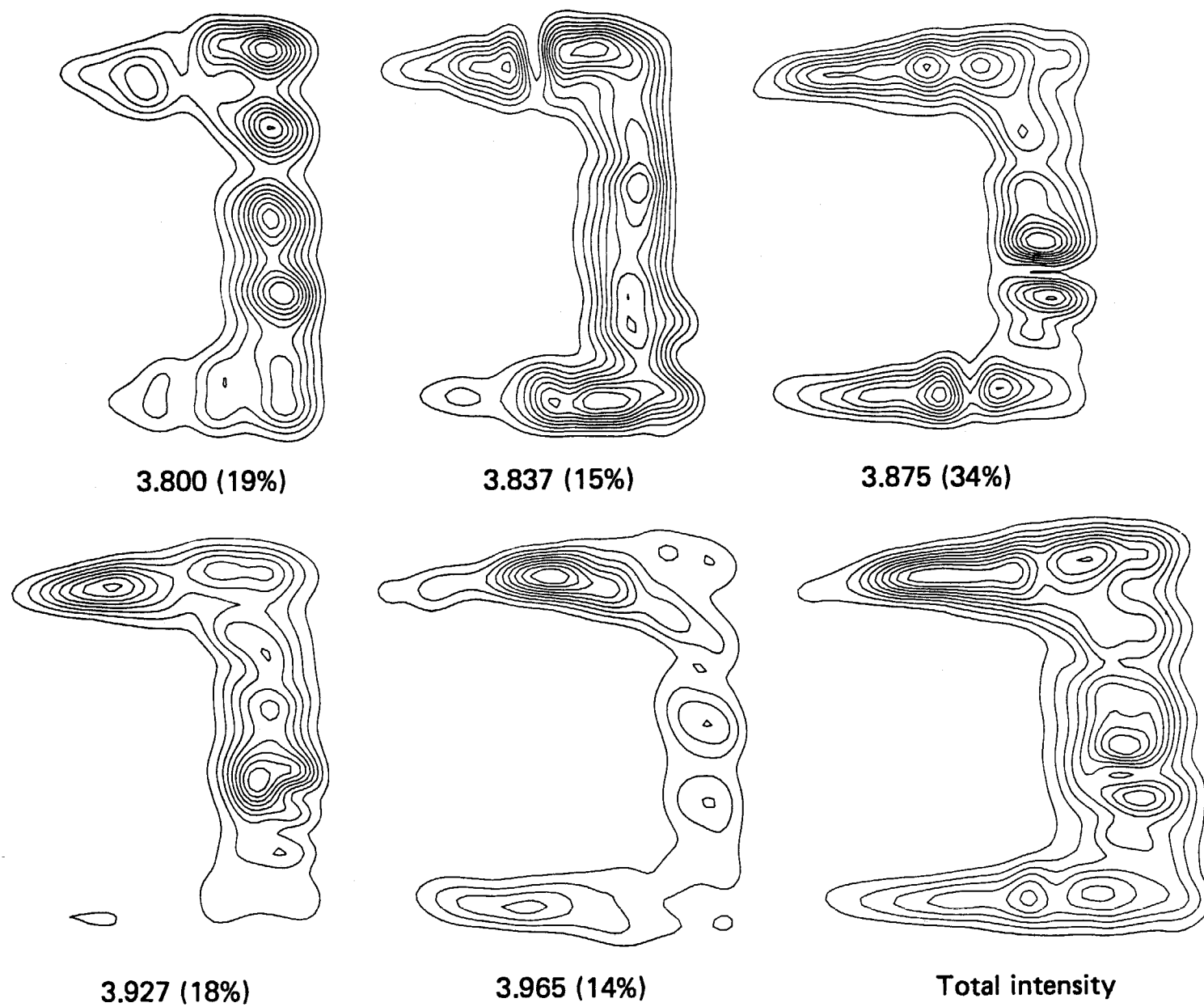


3.875 μ early data

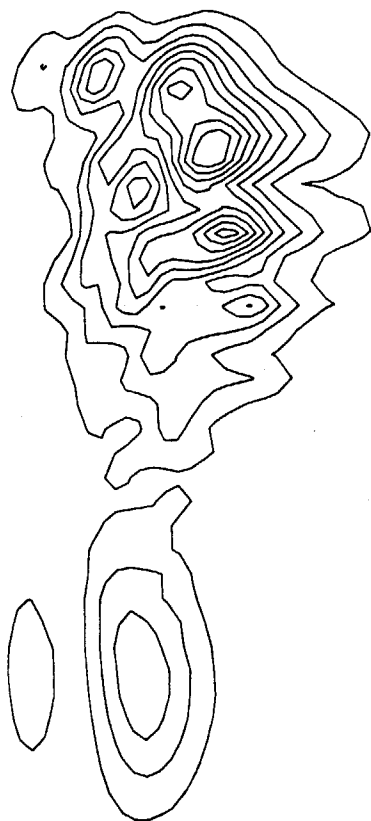


3.875 μ with
improved optics

Figure 3

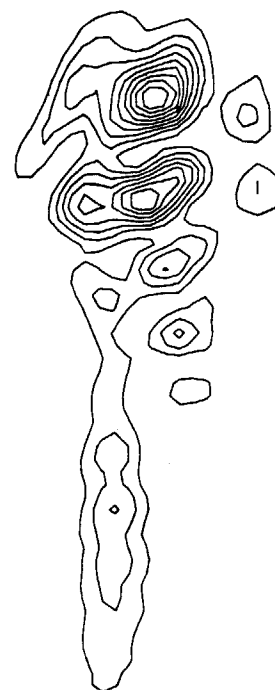


Multiple line



Area 16.8

Power-weighted average



Area 10.7

Figure 4

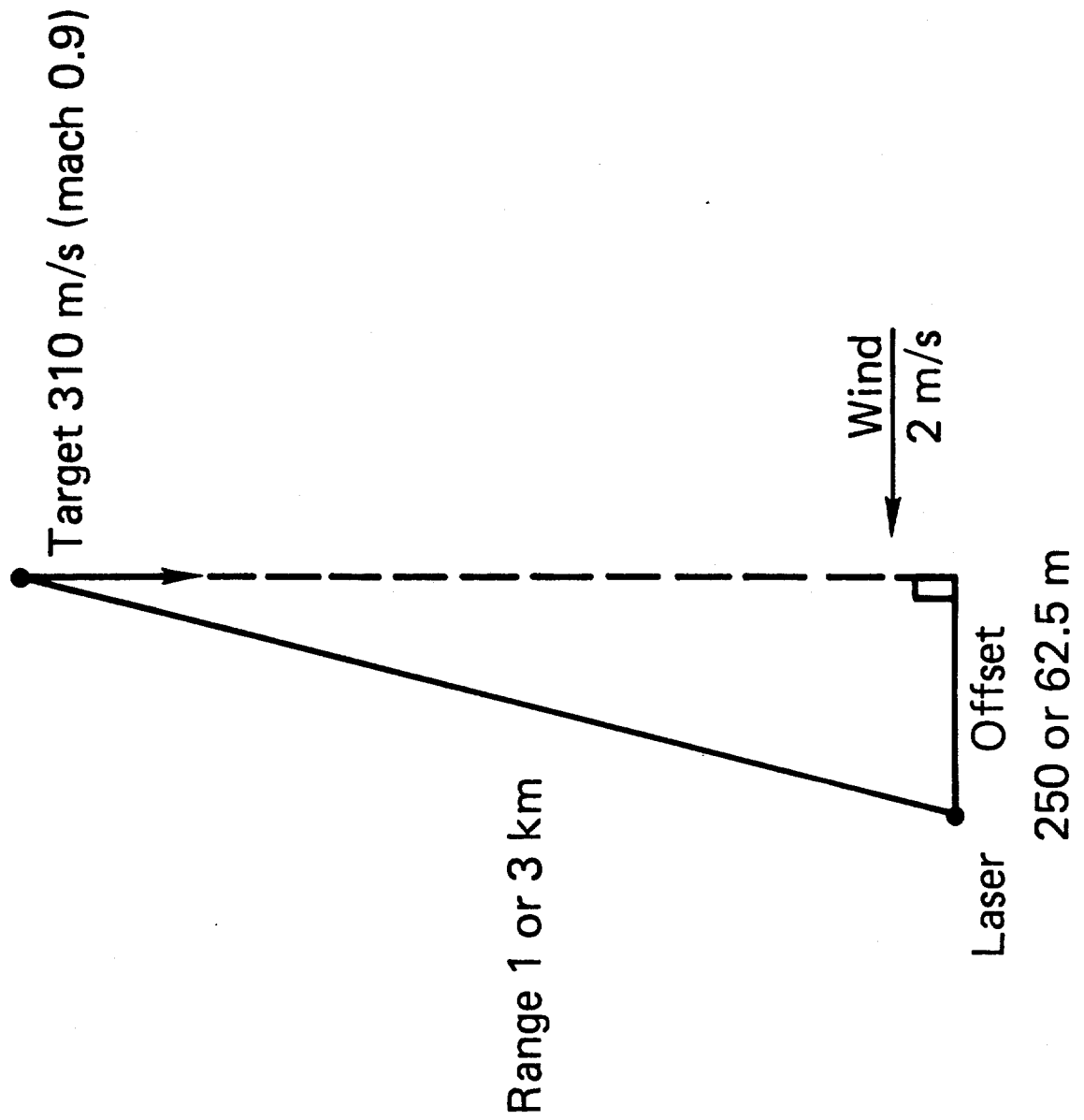


Figure 5

Figure 6

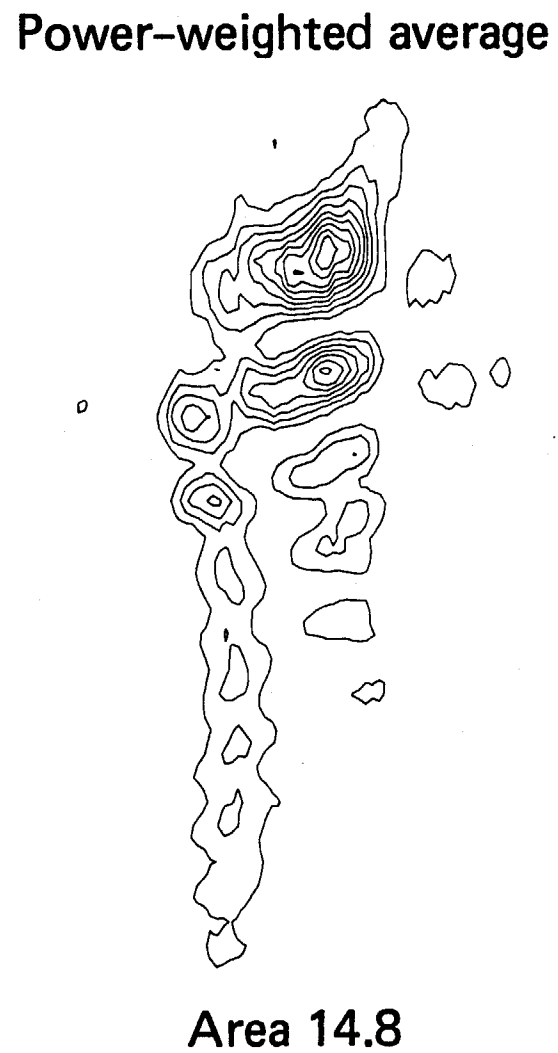
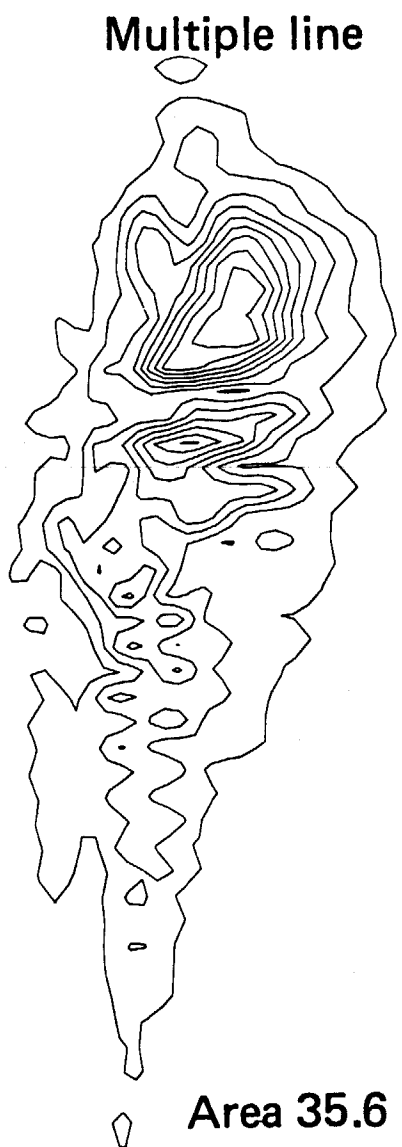


Figure 7



Power-weighted average

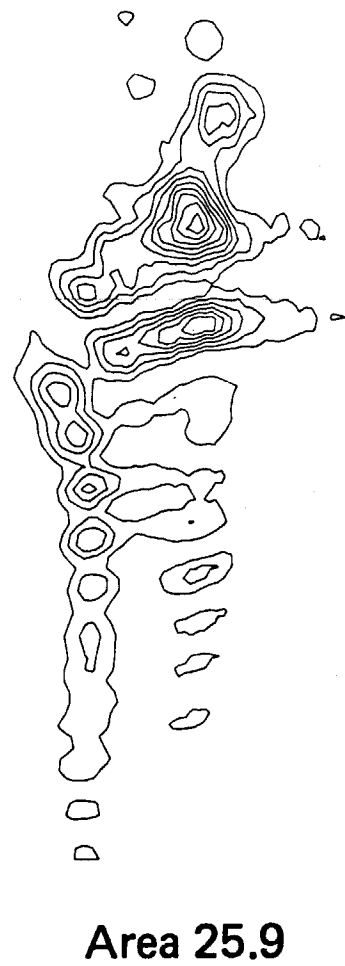


Figure 8

Multiple line



Power-weighted average



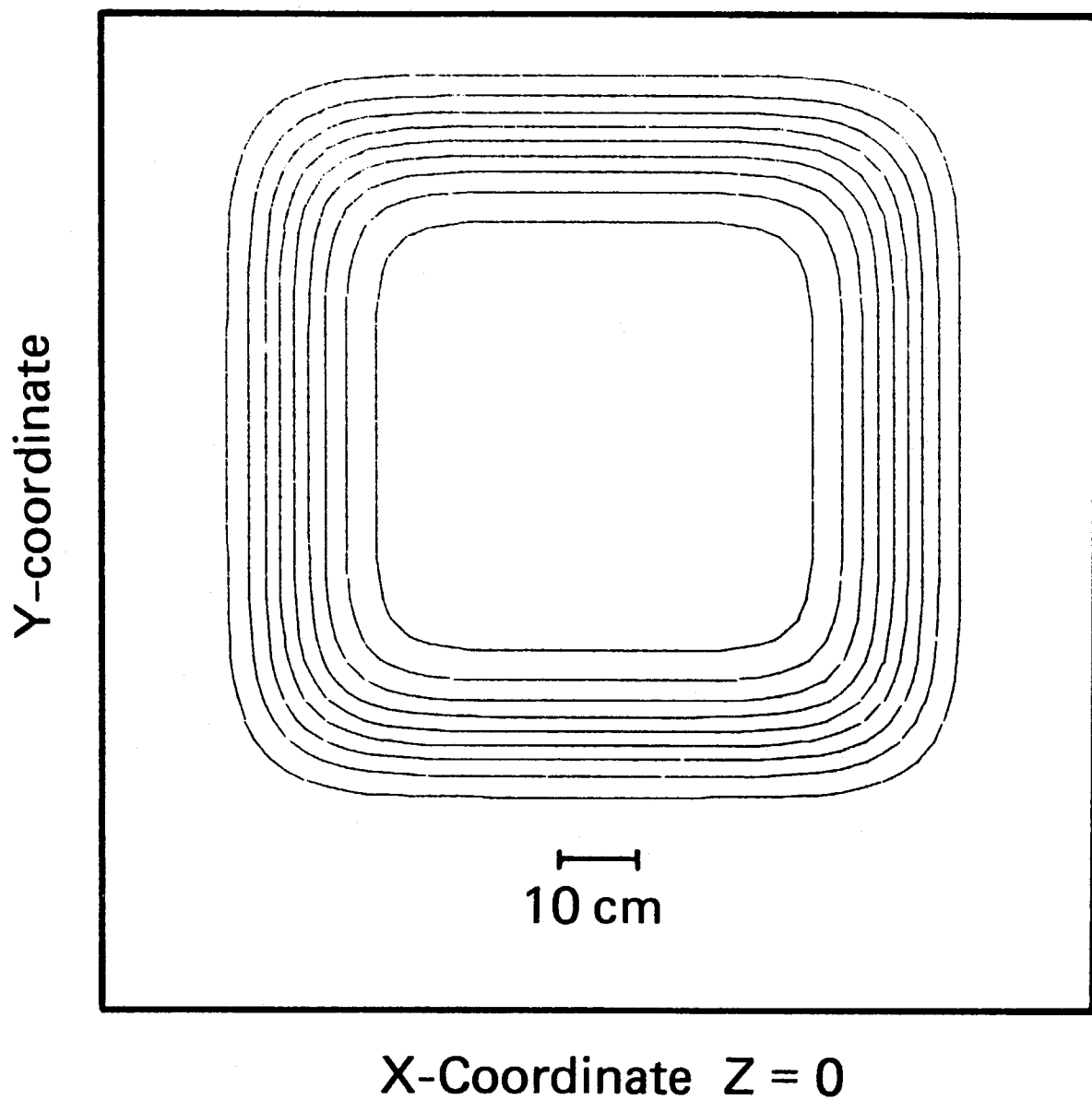
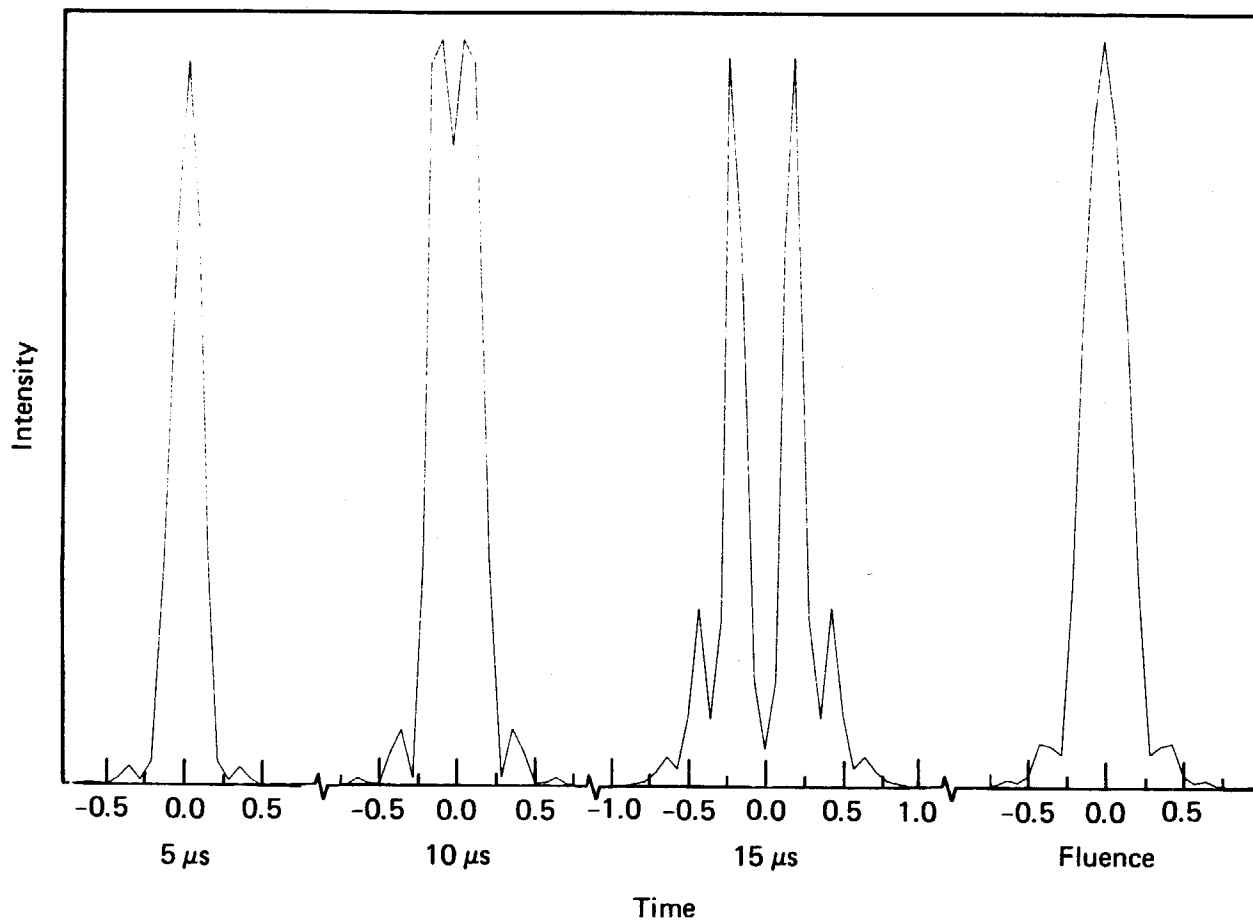


Figure 9

Figure 10



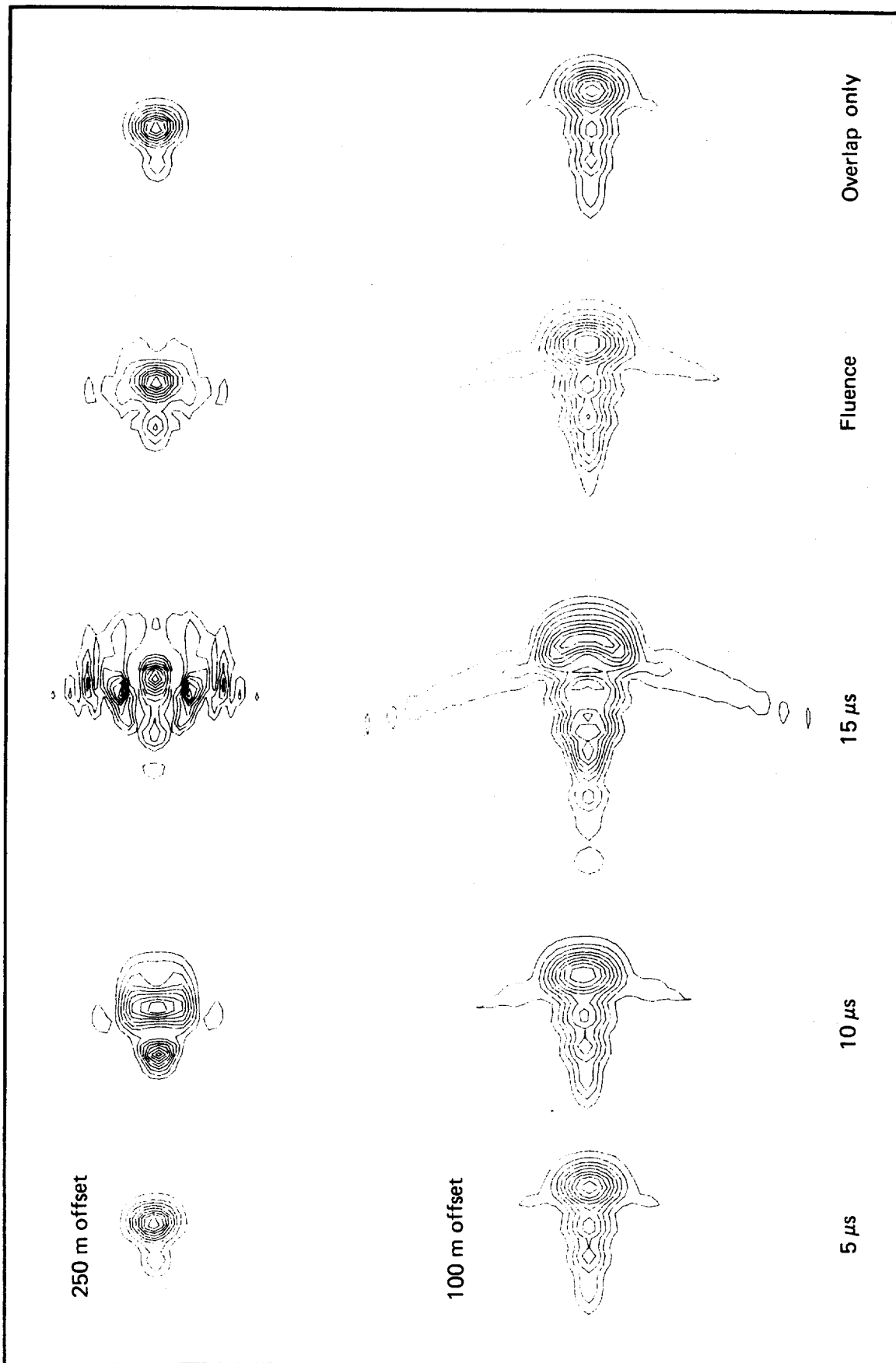
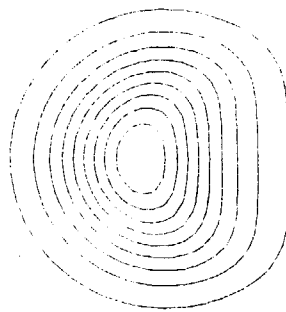
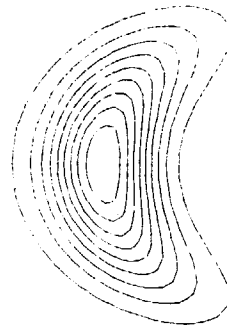


Figure 11

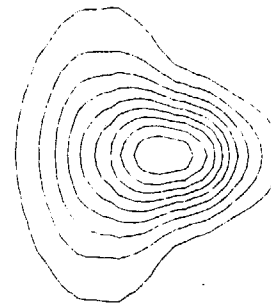
(a) Uncorrected



0.5



0.75



1.0

(b) Corrected



0.5



0.75



1.0

Fractional distance to target

Figure 12

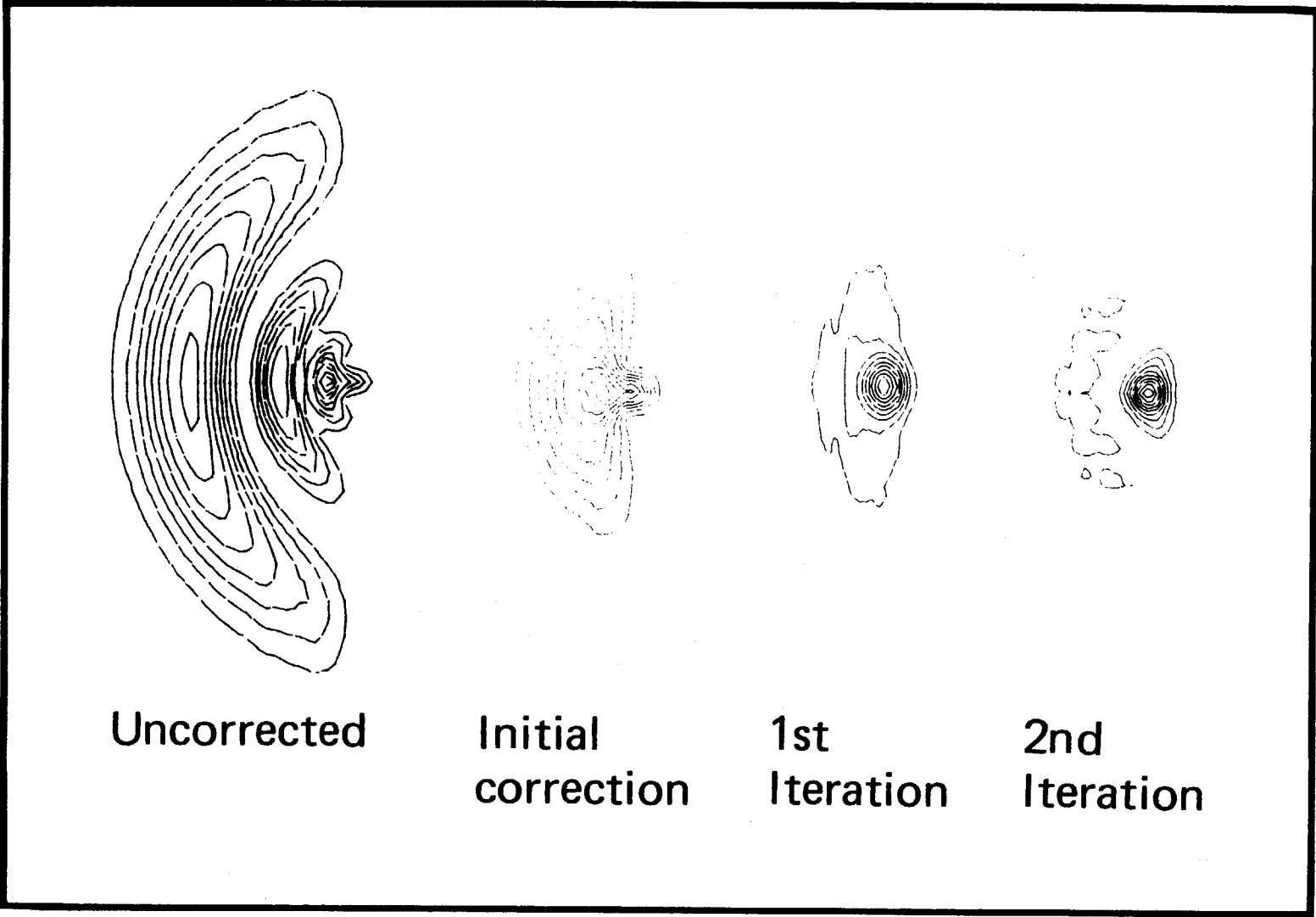


Figure 13

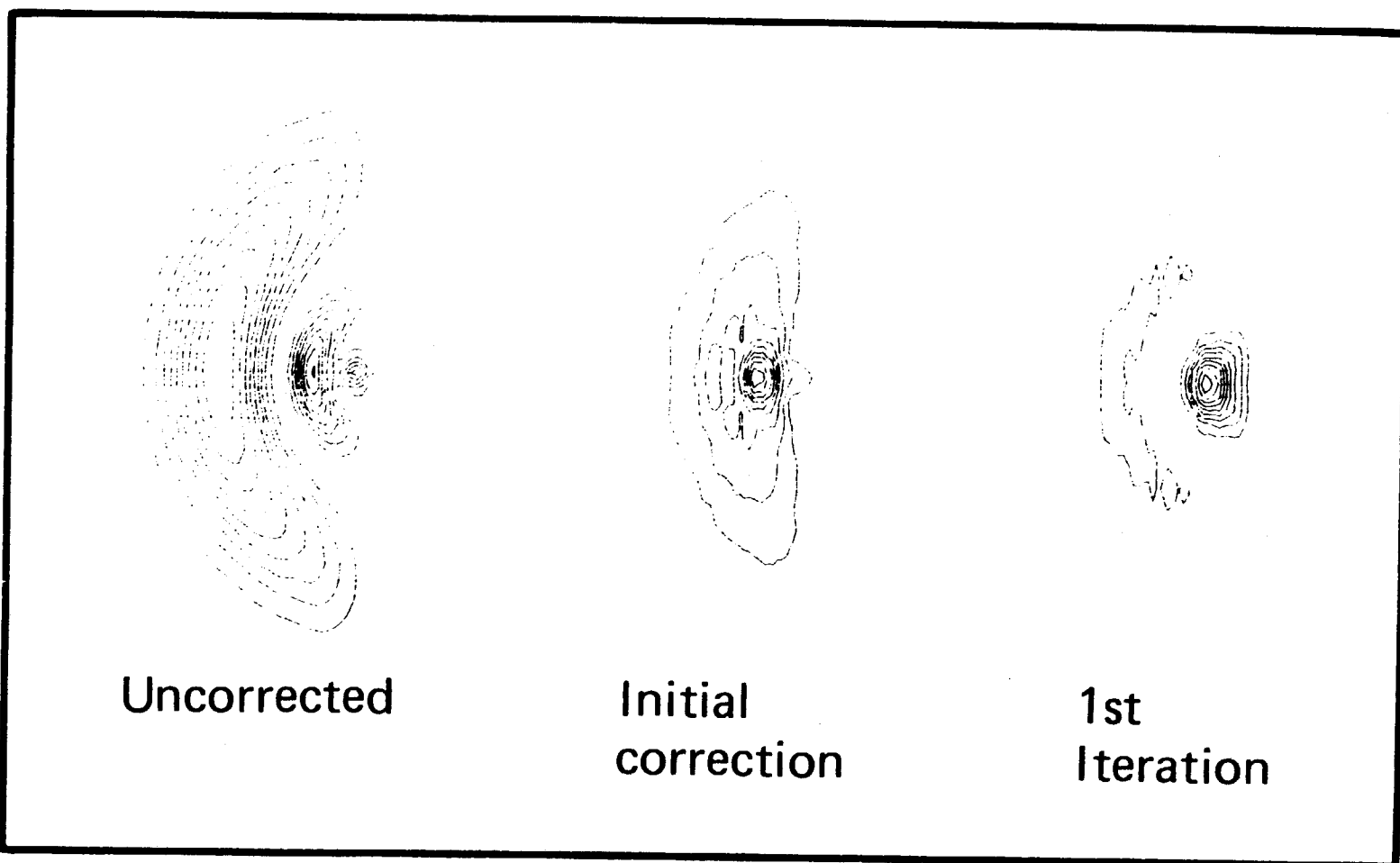


Figure 14

TABLE 1
FITTED ZERNIKE COEFFICIENTS OF 3.875 μ LINES

DATA SET	TILT		REFOCUS	ASTIGMATISM		PRIMARY COMA		TRIFOIL COMA	
	MAGNITUDE	ANGLE (RADIAN)		MAGNITUDE	ANGLE (RADIAN)	MAGNITUDE	ANGLE (RADIAN)	MAGNITUDE	ANGLE (RADIAN)
EARLY	9.01	-2.00	1.22	4.44	-0.20	2.15	1.42	3.19	-0.31
MORE RECENT	10.6	-1.37	5.91	1.90	-0.86	0.41	-0.91	0.99	-0.13

TABLE 2
FITTED ZERNIKE COEFFICIENTS OF FIVE LINE DATA SET

WAVELENGTH (μm)	MAGNITUDE	TILT ANGLE (RADIAN)	REFOCUS	MAGNITUDE	ASTIGMATISM ANGLE (RADIAN)	MAGNITUDE	PRIMARY COMA ANGLE (RADIAN)	MAGNITUDE	TRIFOIL COMA ANGLE (RADIAN)
3.80	6.76	-1.74	-0.10	2.69	-0.66	2.86	1.14	2.84	-0.33
3.837	11.11	-2.14	1.41	3.67	-0.12	2.59	1.51	3.02	-0.45
3.875	9.01	-2.00	1.22	4.44	-0.20	2.15	1.42	3.19	-0.31
3.927	10.72	-2.36	1.04	4.02	-0.23	2.67	1.17	3.89	-0.34
3.965	8.47	-2.47	2.00	3.13	-0.36	2.22	0.94	3.40	-0.35

TABLE 3
PARAMETERS FOR NACL CALCULATIONS

POWER (ARBITRARY UNITS)	38.
SCATTERING COEFFICIENT (KM^{-1})	0.03
MAIN RIDGE LENGTH (CM)	70.

WAVELENGTH (μm)	ABSORPTION COEF. (KM^{-1})	POWER (%)
3.80	0.0353	19
3.837	0.0392	15
3.875	0.0679	34
3.927	0.0438	18
3.965	0.0362	14

TABLE 4

COMPARISON OF POWER WEIGHTED AVERAGE AND MULTIPLE-LINE ON-TARGET AREAS

RANGE	OFFSET	RUN TYPE	WIND DIR	SINGLE-LINE AREAS					FLUENCE AREA	PWA AREA
				3.800	3.837	3.875	3.927	3.965		
1 km		DIFFR		11.1	12.0	13.2	10.4	11.6	16.8	10.7
	250 m	TB	LEFT	11.9	14.8	17.4	14.9	19.2	21.8	14.8
	62.5 m	TB	LEFT	17.5	21.3	29.4	26.8	40.9	35.6	25.9
3 km		DIFFR		96.1	105.4	120.5	98.4	100.1	150.9	94.9
	250 m	TB	LEFT	256	304	402	367	546	503	426
	250 m	TB	RIGHT	644	545	450	514	239	680	527
	250 m	TB	VERTICAL	303	296	404	271	203	501	425

TABLE 5
OVERLAP BLOOMING PLUS T³-BLOOMING OF A SQUARE BEAM

(a) LASER BEAM ATMOSPHERIC AND SCENARIO PARAMETERS		(b) DIMENSIONLESS PARAMETERS	
POWER (P), MW	0.5	$N_0 = 2av/v_0$	20
REPEAT RATE (ν), Hz	50	$N_F = ka^2/R$	47.4
PULSE LENGTH (τ), μs	15	$N_A = \alpha R$	0.472
BEAM SIZE (2a), cm	80	$N_D = \frac{\gamma-1}{2} \frac{\alpha P}{v_0} \frac{\partial \epsilon}{\partial \rho} \frac{kR}{a} =$	280
BEAM SHAPE	$\exp[-(x/a)^6 - (y/a)^6]$	$N_\omega = \omega R/v_0$	7.78, 19.4
WAVE LENGTH, μm	10.6		
WIND SPEED (v_0), m/s	2		
TARGET SPEED, m/s	311 [0.9 c_s]		
ABSORPTION COEFFICIENT (α), km^{-1}	0.236		
SLEWING RATE, mrad/s	7.78, 19.4		
RANGE AND FOCAL DISTANCE (R), km	2		

TABLE 6
COMPARISON OF GAUSSIAN AND SQUARE BEAM T^3 -BLOOMING AND OVERLAP PLUS T^3 -BLOOMING

DESCRIPTION	SQUARE BEAM			GAUSSIAN BEAM	
	OFFSET (m)	AREA (cm ²)	MAXIMUM INTENSITY (kW/cm ²)	AREA (cm ²)	MAXIMUM INTENSITY (kW/cm ²)
DIFFRACTION LIMIT	--	3.5	60.7	3.6	60.7
T^3 -BLOOMING	--	8.5	25.3	9.4	28.7
OVERLAP BLOOMING	250	10.4	26.0	60.5	8.4
T^3 PLUS OVERLAP	250	27.4	11.6	62.5	9.8
OVERLAP BLOOMING	100	33.9	9.9	268	4.6
T^3 PLUS OVERLAP	100	45.2	6.4	250	4.5

TABLE 7

COMPARISON OF FLECK-MORRIS THIN-LENS TO RETURN-WAVE ADAPTIVE-OPTICS CORRECTION

DIMENSIONLESS PARAMETERS				BEAM SHAPE	RELATIVE AREAS			RELATIVE INTENSITIES		
N_F	N_A	N_ω	N_D		UNCORRECTED	R-W	F-M	UNCORRECTED	R-W	F-M
103.3	0.12	10	135	UNIFORMLY CIRCULAR	3.80	3.12	3.38	0.280	0.351	0.365
103.3	0.12	30	450	UNIFORMLY CIRCULAR	4.96	3.53	4.12	0.224	0.349	0.263
18.3	0.40	8	106	TRUNCATED GAUSSIAN	5.28	2.82	3.03	0.195	0.361	0.397
43.3	0.183	~ 82	~ 851 ^a	UNIFORMLY CIRCULAR	6.80	3.46	3.55	0.271	0.428	0.473
9.08	0.40	0	17.8 ^b	INFINITE GAUSSIAN	2.03	1.02	1.09	0.518	0.986	0.934

^aNONCOPLANAR CALCULATION: N_ω AND N_D DEFINITIONS ARE NEBULOUS VALUES SHOWN FOR ROUGH COMPARISON ONLY.

^bMULTIPULSE STEADY-STATE CALCULATION: $N_0 = 2r/V_0\Delta t = 4$.